

Supporting information

Molecular Polarons Coupling-enhanced CO₂ Photocatalytic Reduction on the Copper Phthalocyanine/NiMgFe-Layered Double Hydroxides Nanocomposites

Yuxian Li^a, Wenli Su^b, Xiaoyan Wang^a, Jun Lu^{*a}, Wenkai Zhang^{*b}, Shuo Wei^{*c}

^aState Key Laboratory of Chemical Resource Engineering and College of Chemistry, Beijing University of Chemical Technology, P. Box 98, Beisanhuan East Road 15, Beijing 100029, P. R. China.

^bDepartment of Physics and Applied Optics Beijing Area Major Laboratory, Center for Advanced Quantum Studies, Beijing Normal University, Xinjiekou Outside Street 19, Beijing 100875, China

^cCollege of Chemistry, Beijing Normal University, Xinjiekou Outside Street 19, Beijing 100875, P. R. China

*E-mail (J. Lu): lujun@mail.buct.edu.cn *E-mail (W.K. Zhang): wkzhang@bnu.edu.cn *E-mail (S. Wei): vshuo@bnu.edu.cn

1. Materials
2. Experimental Section
3. Computational Methods
4. Table and Figure

Table S1. Different mole ratio of NMF-LDHs tested by ICP-AES.

Table S2. Metal ion content before and after self-assembly tested by ICP-AES.

Table S3. The fitting radiative lifespan of NMF-LDHs and CuPcS/NMF-LDHs in TRPL test.

Table S4. The fitting lifespan of NMF-LDHs and CuPcS/NMF-LDHs in fs-TA test.

Table S5. Photocatalytic test results for the systems irradiated by UV-vis light for 5 h.

Table S6. The photocatalytic performance comparison of CO₂ reduction over various catalysts.

Figure S1. (A) The DFT calculation of different molar ratio of Ni²⁺: Mg²⁺: Fe³⁺. (B) The surface area curves of AMO-NMF-LDHs and Bulk-NMF-LDHs.

Figure S2. The scanning electron microscope (SEM) images of catalysts (A) NMF-LDHs; (B) CuPcS/NMF-LDHs. The EDS of (C) NMF-LDHs; (D) CuPcS/NMF-LDHs.

Figure S3. The UV-vis absorption spectra of (A) different concentrations of CuPcS solution. (B) Compare the absorption before and after the load.

Figure S4. The zeta potential of (A) self-assembly process, (B) 1.6 wt% CuPcS, (C) NMF-LDHs, CuPcS/NMF-LDHs (D) 0.4 wt%, (E) 0.6 wt%, (F) 0.8 wt%, (G) 0.8 wt%, (H) 1.0 wt% and (I) 1.2 wt%.

Figure S5. The Raman spectra of NMF-LDHs and CuPcS/NMF-LDHs.

Figure S6. The UV-vis diffuse reflectance spectra were fitted with Kubelka-Munk formula and Tauc's plot to estimate the band gap (A) NMF-LDHs and (B) CuPcS. MS curves of NMF-LDHs at different frequencies (C) 1000 Hz, (D) 2000 Hz, (E) 3000 Hz, (F) 4000 Hz, (G) 10000 Hz. MS curves of CuPcS at different frequencies (H) 1000 Hz, (I) 2000 Hz, (J) 3000 Hz, (K) 4000 Hz, (L) 10000 Hz.

Figure S7. (A) The semiconductor energy level diagram of NMF-LDHs and CuPcS. The EIS test of NMF-LDHs

and the the loading of different concentrations of CuPcS (0.4 wt%, 0.6 wt%, 1.2 wt%, 1.6 wt%, 2.0 wt%) on NMF-LDHs in (B) dark or (C) light.

Figure S8. XPS spectra of the NMF-LDHs and CuPcS/NMF-LDHs (A) Cu 2p; (B) N 1s; (C) O 1s.

Figure S9 (A) The lifetimes of NMF-LDHs at 700 nm with 400 nm laser excitation by fitting the bi-exponential. (B) TA spectra of NMF-LDHs with 630 nm laser excitation at the different delay times. (C) Comparison of steady-state and transient absorption spectra of CuPcS. The lifetimes of (D) CuPcS and (E) CuPcS/NMF-LDHs with 630 nm laser excitation by fitting the bi-exponential. TA spectra of Pcs with 400 nm laser excitation (F) and 630 nm laser excitation (G) at the different delay times. TA spectra of Pcs/NMF-LDHs with 400 nm laser excitation (H) and 630 nm laser excitation (I) at the different delay times.

Figure S10. GC standard curve for the quantitative determination of pure (A) CO and (B) CH₄ by external standard method. (C) The isotope experiments of photocatalytic CO₂ reduction with ¹³CO₂.

Figure S11. (A) Screening of photocatalytic reduction performance of samples. (B) Selection of photocatalytic reduction performance of samples. (C) The yields of CO and CH₄ for samples. (D) The yields of CO and CH₄ for samples. (E) The yields of CH₄ for samples within 5 hours. (F) performing blank and control experiments under the same experimental conditions.

Figure S12. Schematic of the self-assembled molecular orientation of CuPcS with NMF-LDHs. (A) CuPcS molecular structure, (B) horizontal arrangement, (C) vertical arrangement, (D) mixed arrangement, (E) vertical arrangement of multiple CuPcS.

Figure S13. (A) The 2D spectra of *in-situ* FTIR of the CuPcS/NMF-LDHs. (B) The *in-situ* FTIR of the NMF-LDHs. (C) EPR of CuPcS added DMPO to test the ·OH and ·O₂⁻ signals at room temperature.

1. Materials:

Analytically pure nickel nitrate hexahydrate (Ni(NO₃)₂·6H₂O), magnesium nitrate hexahydrate (Mg(NO₃)₂·6H₂O) and ferric nitrate nine hydrate (Fe(NO₃)₃·9H₂O) from Aladdin. The sodium carbonate and sodium bicarbonate are both 99.9% pure from Titan. Copper tetrasulfonate phthalocyanine (CuPcS) from Shanghai Yuanye is of superior purity. The purity of anhydrous ethanol and methanol is 95% and 99% respectively.

2. Experimental section

2.1 Electrochemical measurement:

A 10 mg catalyst sample was dispersed in 485 μ l of deionized water, 485 μ l of ethanol, and 30 μ l of Nafion was added to ultrasonically disperse for 10 min. Then the dispersion was uniformly applied on the glassy carbon electrode to form a sample film, which was ready for measurement. A three-electrode system with a rotating ring disk, in which the counter and reference electrodes were graphite and saturated glycury electrodes, respectively, and the electrolyte solution was 0.1 M Na₂SO₄ (pH = 6.8). Dark conditions were tested under alternating voltage only, and light conditions were introduced with a 300 W xenon lamp. Electrochemical impedance spectroscopy (EIS) test, transient photocurrent corresponding, Mott-Schottky curves were studied with an electrochemical workstation (660E, Shanghai C&H Instruments).

2.2 Photocatalytic CO₂ reduction measurement:

30 mg of photocatalyst was dispersed in 30 ml of deionized water and 5 ml of triethanolamine ultrasonicated for 30 min. Then the dispersion was poured into a 100 ml quartz reaction cell, sealed and continuously ventilated with high purity CO₂ gas for 30 min. 300 W xenon lamp was used for overhead illumination, and condensed water was used to keep the whole catalytic reaction at room temperature. The headspace gas products were monitored every 1 h using gas chromatography (GC-7920, TDX-01) with flame ionization detector (FID) and N₂ as the

carrier gas. To ensure the accuracy of the photocatalytic measurement data, at least three parallel experiments were performed for each photocatalyst. For the stability experiments of the photocatalysts, four experiments were performed under the same test conditions as above. Isotope experiments of CO₂ were performed by drumming in ¹³CO₂ gas and analyzed by gas-phase mass spectrometry (GCMS-QP2020).

2.3 *In-situ* Fourier transform infrared spectroscopy measurement (*in-situ* FTIR):

Using an American Nicolet 6700 infrared spectrometer equipped with a BaF₂ window and an MCT detector, the instrument has a measurement range of 4000 ~ 400 cm⁻¹. The measurements were performed in diffuse reflection mode.

Sample pretreatment: The photocatalyst was pretreated using high purity Ar and programmed warming to remove the adsorbed CO₂ and H₂O on the surface. To be specific, the powder photocatalyst was placed in the *in-situ* cell and flattened it. Ar was continuously introduced and maintained at a ramp rate of 10°C/min from 25°C to 100 °C for 40 min. Subsequently, it was left to cool to room temperature and a blank background was collected.

CO₂ *in-situ* reaction operation: High-purity CO₂ and trace water were blown into the *in-situ* reaction cell by the bubbling method, and the gas flow rate of CO₂ was 10 ml/min. The first spectrum was collected and recorded as 0 min, followed by the top illumination of the *in-situ* cell with 300 W xenon lamp. The spectrum was collected at an interval of 2 min, and the reaction was carried out for 30 min. In order to keep the temperature of the *in-situ* cell at room temperature, the whole reaction was maintained by condensing circulating water.

3. Computational Methods

The spin-polarized density functional theory (DFT) calculations were performed at the level of generalized gradient approximation (GGA) Perdew-Burke-Ernzerhof (PBE) through the CASTEP module in Materials Studio 5.5 (Accelrys software Inc., San Diego, CA). The ultrasoft pseudopotentials were used to characterize the ionic cores of Ni, Cu, O. The cut-off energy and *k*-points were set as 400 eV and 1 × 1 × 1, respectively. BFGS geometry scheme was used to search the minimum point of the potential energy surface. The three convergence criteria of geometric optimization are as follows: (1) the energy tolerance of 1×10⁻⁵ eV/atom; (2) maximum displacement tolerance of 1×10⁻³ Å; (3) maximum force tolerance of 3×10⁻² eV/Å.

3.1 Calculation details:

Kubelka-Munk formula and Tauc's plot to estimate the band gap as follow:

$$(ahv)^{1/n} = A (hv - E_g)$$

Calculate $(ahv)^{1/n}$ and hv respectively, where for the direct band gap $n = 1/2$ and for the indirect band gap $n = 2$. By plotting hv and $(ahv)^{1/n}$ as transverse and vertical coordinates, and extrapolating from the x-axis intercept, the band gap energy was obtained. Among them, A , h , α , v , and E_g were proportionality constant, Plank constant, absorption coefficient, light frequency, and band gap energy, respectively.

The valence band potential (E_{VB}) can be calculated as:

$$E_g = E_{CB} - E_{VB}$$

Calculations based on the escape work (Φ), secondary electron cutoff edge (E_{cutoff}) and valence band top position (E_{VB}^F) are as follows, where the light source is He I, the $h\nu$ is 21.22 eV.

$$E^{\text{vac}}_{\text{HOMO-CuPcS}} = -IP = -(\Phi + E_{VB}^F) = -(h\nu - E_{cutoff} + E_{VB}^F)$$

$$E^{\text{NHE}}_{\text{HOMO-CuPcS}} = -4.5 - E^{\text{vac}}_{\text{HOMO-CuPcS}}$$

Time-resolved photoluminescence (TRPL) spectra and the transient absorption spectra (TAS) were used to get time decay curves. The decay curves can be fitted by the multi-exponential equation below:[1]

$$I(t) = I_0 + A_1 \exp(-t/\tau_1) + A_2 \exp(-t/\tau_2)$$

The average lifetimes (τ_a) can be calculated as follows:

$$\tau_a = \frac{A_1 \tau_1^2 + A_2 \tau_2^2}{A_1 \tau_1 + A_2 \tau_2}$$

Table S1. Different mole ratio of NMF-LDHs tested by ICP-AES.

	mean value/(ppm)			standard deviation/(ppm)		
	Fe	Ni	Mg	Fe	Ni	Mg
1:1:1	1.125	1.321	1.089	0.015	0.033	0.013
2:1:1	2.238	1.115	0.996	0.011	0.021	0.025
1:2:1	1.052	2.038	1.091	0.0179	0.008	0.022

Table S2. Metal ion content before and after self-assembly tested by ICP-AES.

	mean value/(ppm)				standard deviation/(ppm)			
	Fe 2259	Ni 2216	Mg 2790	Cu 3247	Fe 2259	Ni 2216	Mg 2790	Cu 3247
NMF-LDHs	1.459	1.069	1.111	0	0.345	0.035	0.068	0
CuPcS/NMF-LDHs	1.216	1.088	1.213	0.039	0.015	0.042	0.245	0.01

Table S3. The fitting radiative lifespan of NMF-LDHs and CuPcS/NMF-LDHs in TRPL test.

		A_1	$\tau_1(\text{ns})$	A_2	$\tau_2(\text{ns})$	$\tau_a(\text{s})$
NMF-LDHs	302 nm	95.191	869.27	31.682	12355.88	44.32
CuPcS/NMF-LDHs	302 nm	78.962	549.58	20.841	12790.43	24.06

Table S4. The fitting lifespan of NMF-LDHs and CuPcS/NMF-LDHs in fs-TA test.

Excitation wavelength	Detection wavelength	Photocatalyst	A_1	$\tau_1(\text{ps})$	A_2	$\tau_2(\text{ps})$	$\tau_a(\text{ps})$
400nm	590 nm	CuPcS/NMF-LDHs	2.3675	31.243	0.655	1759.067	1645.282
	660 nm		0.599	1680.8701	0.372	49.049	1651.873
	800 nm		-0.539	1016.648	-0.338	110.499	1017.457
	700 nm		-0.546	1397.739	-0.145	1021.102	1368.257
630 nm	590 nm	CuPcS/NMF-LDHs	0.137	145.459	0.665	2119.182	2091.738
	660 nm		1.407	57.509	18.357	58251.499	58247.163

540 nm	CuPcS	0.109	37.631	0.672	1562.303	1556.172
---------------	--------------	-------	--------	-------	----------	----------

Table S5. Photocatalytic test results for the systems irradiated by UV-vis light for 5 h.

photocatalyst	The yields of CO ($\mu\text{mol/g}\cdot\text{h}$)	The yields of CH ₄ ($\mu\text{mol/g}\cdot\text{h}$)	TCEN ^[a] ($\mu\text{mol/mg}$)	Activity improvement rate ^[b] (%)	Apparent quantum yield (AQY, %)
NMF-LDHs	72.953	5.576	6.351	-	0.645
CuPcS	30.035	1.896	2.508	-	0.255
0.4 wt% CuPcS/NMF-LDHs	79.355	9.190	6.847	7.810	0.787
0.6 wt% CuPcS/NMF-LDHs	51.345	5.838	4.979	-21.603	0.560
1.2 wt% CuPcS/NMF-LDHs	89.131	18.748	10.942	72.288	1.111
1.6 wt% CuPcS/NMF-LDHs	122.657	18.891	13.215	108.077	1.342
2.0 wt% CuPcS/NMF-LDHs	111.220	15.380	11.516	81.326	1.170
1.6 wt% CuPcS/NMF-LDHs (1:9)	404.660	32.814	35.728	462.557	3.630
1.6 wt% CuPcS/NMF-LDHs (3:7)	635.641	76.342	62.733	887.766	6.375
1.6 wt% CuPcS/NMF-LDHs (5:5)	543.841	64.081	53.344	739.931	5.421
1.6 wt% CuPcS/NMF-LDHs (7:3)	481.948	52.887	46.233	627.964	4.458
1.6 wt% CuPcS/NMF-LDHs (9:1)	467.494	40.334	41.922	560.085	3.363
1.6 wt% Pcs/NMF-LDHs	150.924	7.257	11.997	88.899	1.219

The potoreduction CO₂ results can be calculation by equation below:

$$^{[a]} \text{TCEN} = \frac{\sum (n_{\text{production}} \times n_{\text{electrons}})}{m_{\text{cat.}}}$$

TCEN was represented the total number of electrons actually consumed in photocatalytic CO₂ reduction, n_{production} and n_{electrons} were the yields of actual product of CO₂ reduction and the moles of electrons reacted to form a mole product (CO: n_{electrons} = 2; CH₄: n_{electrons} = 8), respectively.

$$^{[b]} \text{Activity improvement rate (\%)} = \frac{\text{TCEN}_{(\text{catalysts})} - \text{TCEN}_{(\text{NMF - LDHs})}}{\text{TCEN}_{(\text{NMF - LDHs})}} \times 100\%$$

Quantum Yield (QY) is often used to estimate the efficiency of reactors for formation of the products' yields. QY shows the number of times a reaction occurs per photon absorbed by the system during any radiation-induced process. The number of incident photons can be estimated by an intensity meter. Nevertheless, it is difficult to determine the exact measure of photons absorbed by a photocatalyst due to the scattering. For that reason, the acquired quantum yield is an apparent quantum yield (AQY).¹ The AQY of products can be described as 10 electrons used for production of methane (8 electrons), and carbon monoxide (2 electrons), as follow:²

$$^{[c]}AQY = \frac{CH_4 \text{ yields } (\mu\text{mol}/\text{s}) \times 8 + CO \text{ yields } (\mu\text{mol}/\text{s}) \times 2}{\text{Photon flux } (\mu\text{mol}/\text{s})} \times 100\%$$

where, both, yields of products and photon intensity are in μmol . Photon intensity can be calculated as follow:³

$$\text{Photon flux } (\mu\text{mol}/\text{s}) = \frac{\text{Intensity of light} \times \text{Wavelength}}{\text{Planck constant} \times \text{Photon density}} \times \frac{\text{Incident area}}{\text{Avogadro's constant}}$$

The intensity of the lamp is represented in W m^{-2} , the light wavelength is in meters (m) and the reactor incident area is calculated in m^2 . Planck's constant, Photondensity, and Avogadro's number are with values $6.63 \times 10^{-34} \text{ J}\cdot\text{s}$, $3 \times 10^8 \text{ m}\cdot\text{s}^{-1}$, and $6.63 \times 10^{23} \text{ mol}^{-1}$, respectively.

Table S6. The photocatalytic performance comparison of CO_2 reduction over various catalysts.

photocatalyst	mass	Light source	Hydrogen source	CO production	CH_4 production	Ref.
CuPcS/NMF-LDHs	30mg	Xenon lamp of 300 $\text{mW}\cdot\text{cm}^{-2}$	H_2O	635.641 $\mu\text{mol}/\text{g}_{\text{cat}}\cdot\text{h}$	76.342 $\mu\text{mol}/\text{g}_{\text{cat}}\cdot\text{h}$	This work
CuPc/UCN	20mg	300 W Xenon lamp ($\lambda > 420 \text{ nm}$)	H_2O	9.17 $\mu\text{mol}/\text{g}_{\text{cat}}\cdot\text{h}$	0.91 $\mu\text{mol}/\text{g}_{\text{cat}}\cdot\text{h}$	⁴
g-C₃N₄/CoPc-COOH	50mg	300 W Xenon lamp ($\lambda > 420 \text{ nm}$)	H_2O	646.5 $\mu\text{mol}/\text{g}_{\text{cat}}\cdot\text{h}$	-	⁵
CoPc/α-Fe₂O₃	0.1g	300 W Xenon lamp ($\lambda > 420 \text{ nm}$)	H_2O	15.2 $\mu\text{mol}/\text{g}_{\text{cat}}\cdot\text{h}$	4.7 $\mu\text{mol}/\text{g}_{\text{cat}}\cdot\text{h}$	⁶
FePc/WO₃	0.1 g	300 W Xenon lamp	H_2O	4.3 $\mu\text{mol}/\text{g}_{\text{cat}}\cdot\text{h}$	1.5 $\mu\text{mol}/\text{g}_{\text{cat}}\cdot\text{h}$	⁷
ZnPc/1.5G/BVNS	50mg	300 W Xenon lamp ($\lambda > 420 \text{ nm}$)	H_2O	14.5 $\mu\text{mol}/\text{g}_{\text{cat}}\cdot\text{h}$	11.8 $\mu\text{mol}/\text{g}_{\text{cat}}\cdot\text{h}$	⁸
CuPc/Au-BVNS	50mg	Xenon lamp of 300 $\text{mW}\cdot\text{cm}^{-2}$	H_2O	22.5 $\mu\text{mol}/\text{h}\cdot\text{g}$	2.7 $\mu\text{mol}/\text{g}_{\text{cat}}\cdot\text{h}$	⁹

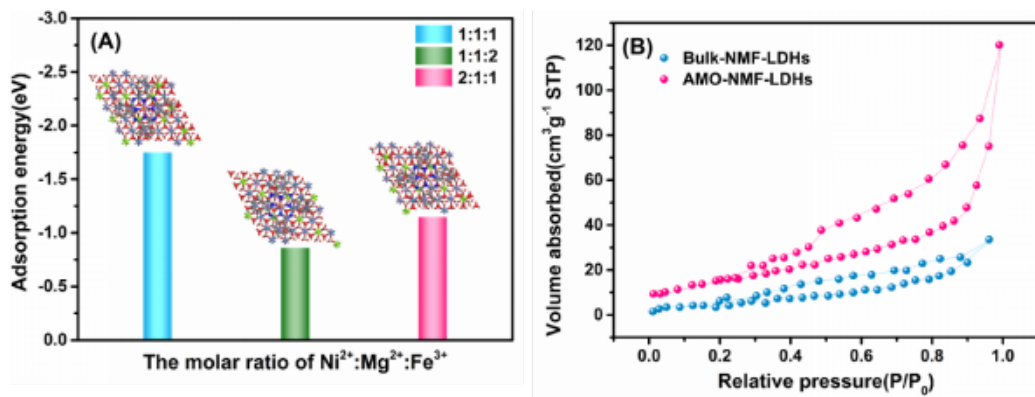


Figure S1. (A) The DFT calculation of different molar ratio of Ni^{2+} : Mg^{2+} : Fe^{3+} . (B) The surface area curves of AMO-NMF-LDHs and Bulk-NMF-LDHs.

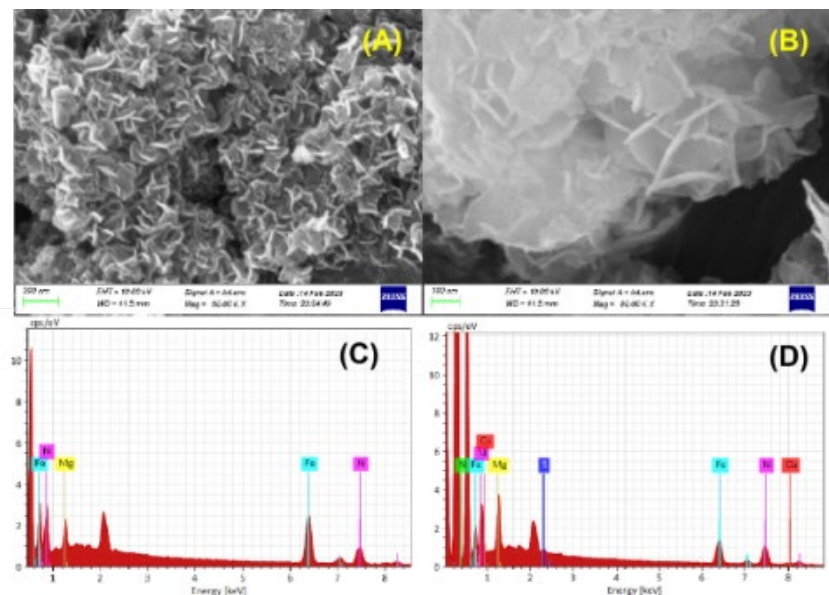


Figure S2. The scanning electron microscope (SEM) images of catalysts (A) NMF-LDHs; (B) CuPcS/NMF-LDHs. The EDS of (C) NMF-LDHs; (D) CuPcS/NMF-LDHs.

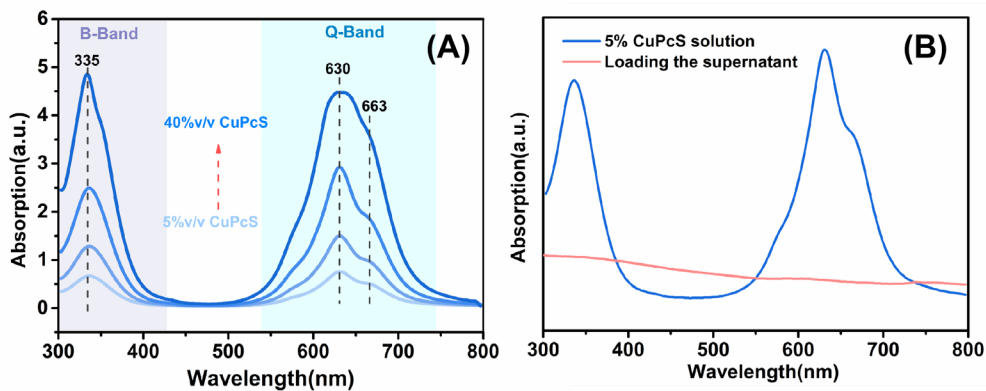


Figure S3. The UV-vis absorption spectra of (A) different concentrations of CuPcS solution. (B) Compare the absorption before and after the load.

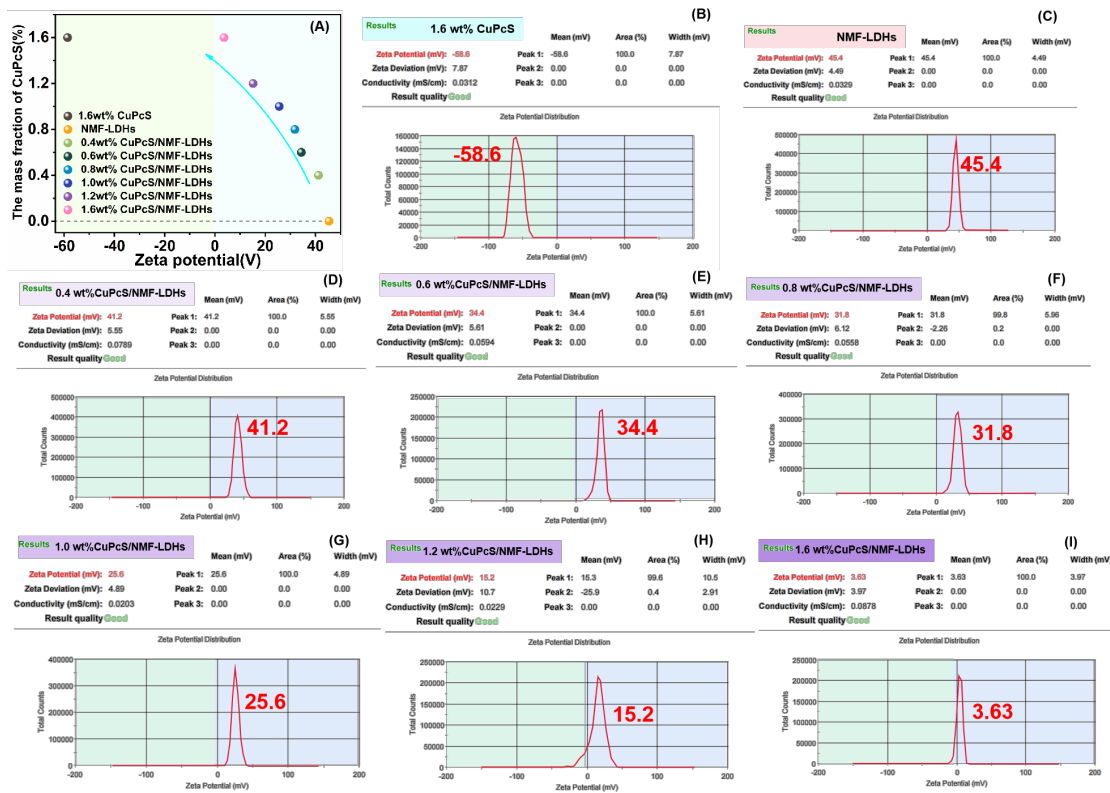


Figure S4. The zeta potential of (A) self-assembly process, (B) 1.6 wt% CuPcS, (C) NMF-LDHs, CuPcS/NMF-LDHs (D) 0.4 wt%, (E) 0.6 wt%, (F) 0.8 wt%, (G) 0.8 wt%, (H) 1.0 wt% and (I) 1.2 wt%.

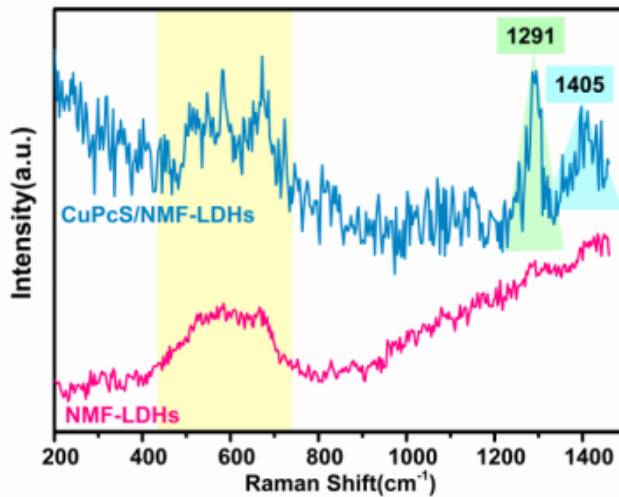


Figure S5. The Raman spectra of NMF-LDHs and CuPcS/NMF-LDHs.

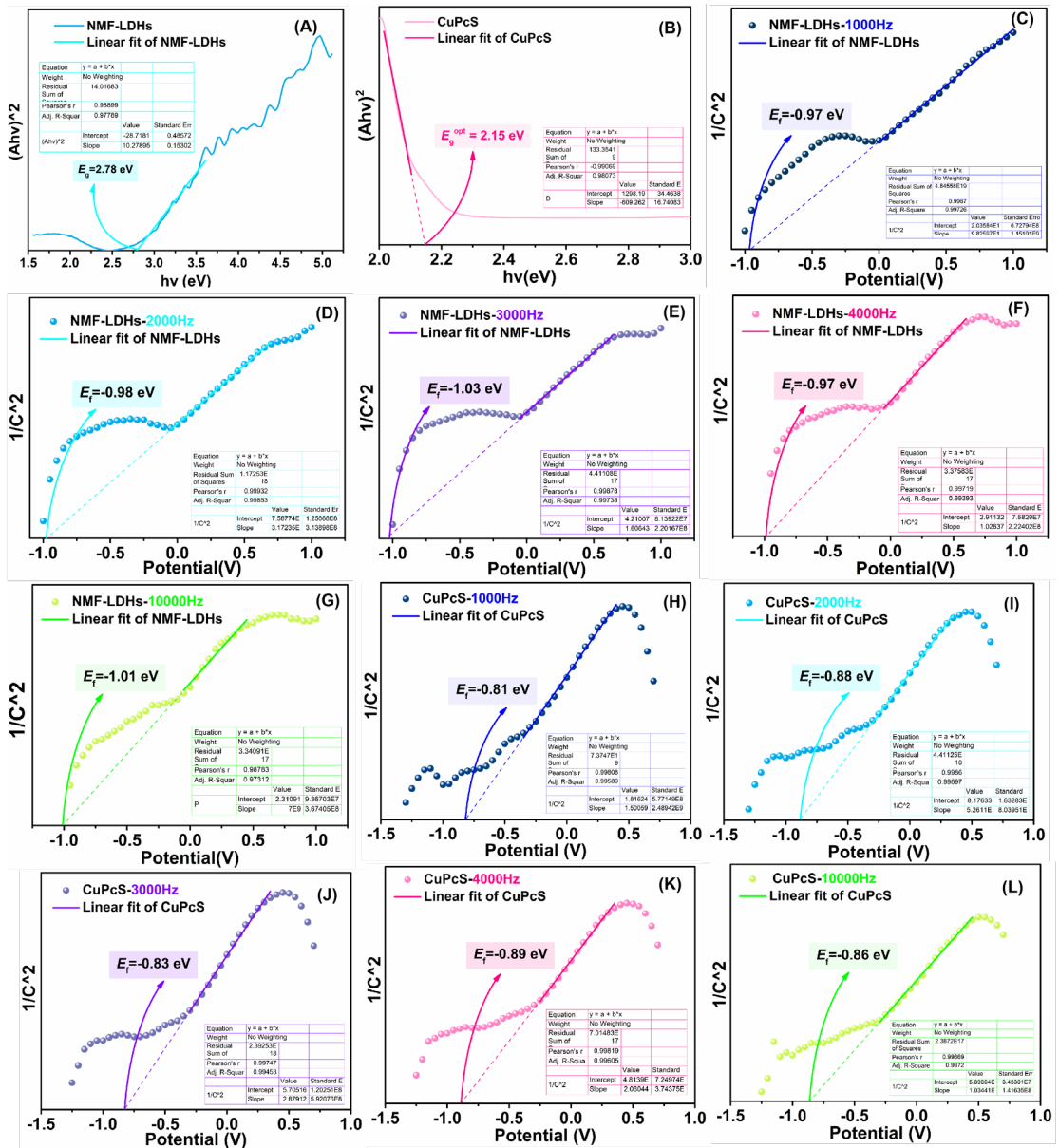


Figure S6. The UV-vis diffuse reflectance spectra were fitted with Kubelka-Munk formula and Tauc's plot to estimate the band gap **(A)** NMF-LDHs and **(B)** CuPcS. MS curves of NMF-LDHs at different frequencies **(C)** 1000 Hz, **(D)** 2000 Hz, **(E)** 3000 Hz, **(F)** 4000 Hz, **(G)** 10000 Hz. MS curves of CuPcS at different frequencies **(H)** 1000 Hz, **(I)** 2000 Hz, **(J)** 3000 Hz, **(K)** 4000 Hz, **(L)** 10000 Hz.

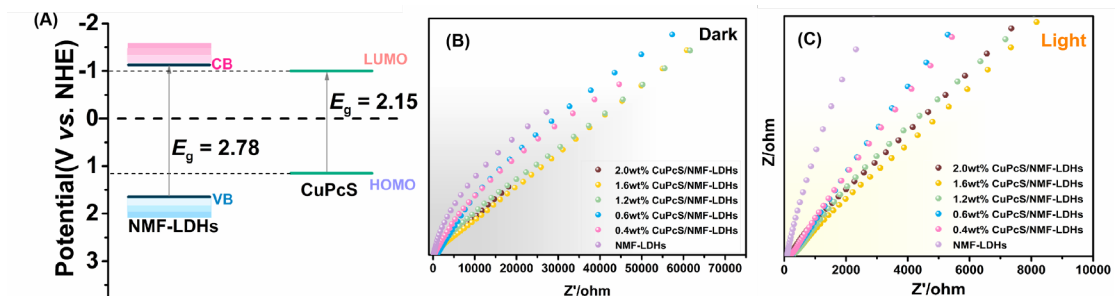


Figure S7. **(A)** The semiconductor energy level diagram of NMF-LDHs and CuPcS. The EIS test of NMF-LDHs and the loading of different concentrations of CuPcS (0.4 wt%, 0.6 wt%, 1.2 wt%, 1.6 wt%, 2.0 wt%) on

NMF-LDHs in (B) dark or (C) light.

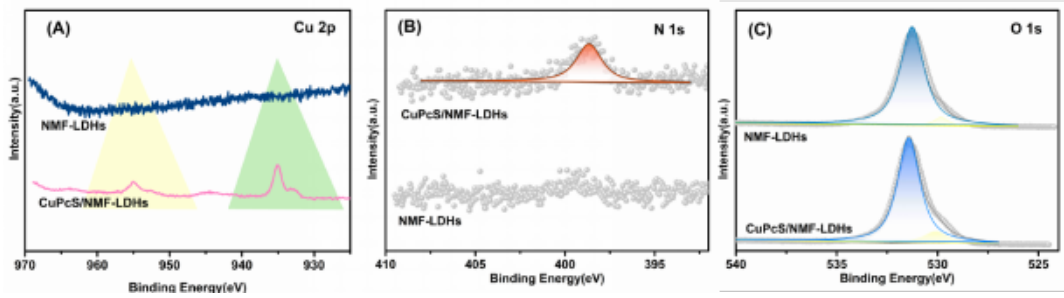


Figure S8. XPS spectra of the NMF-LDHs and CuPcS/NMF-LDHs (A) Cu 2p; (B) N 1s; (C) O 1s.

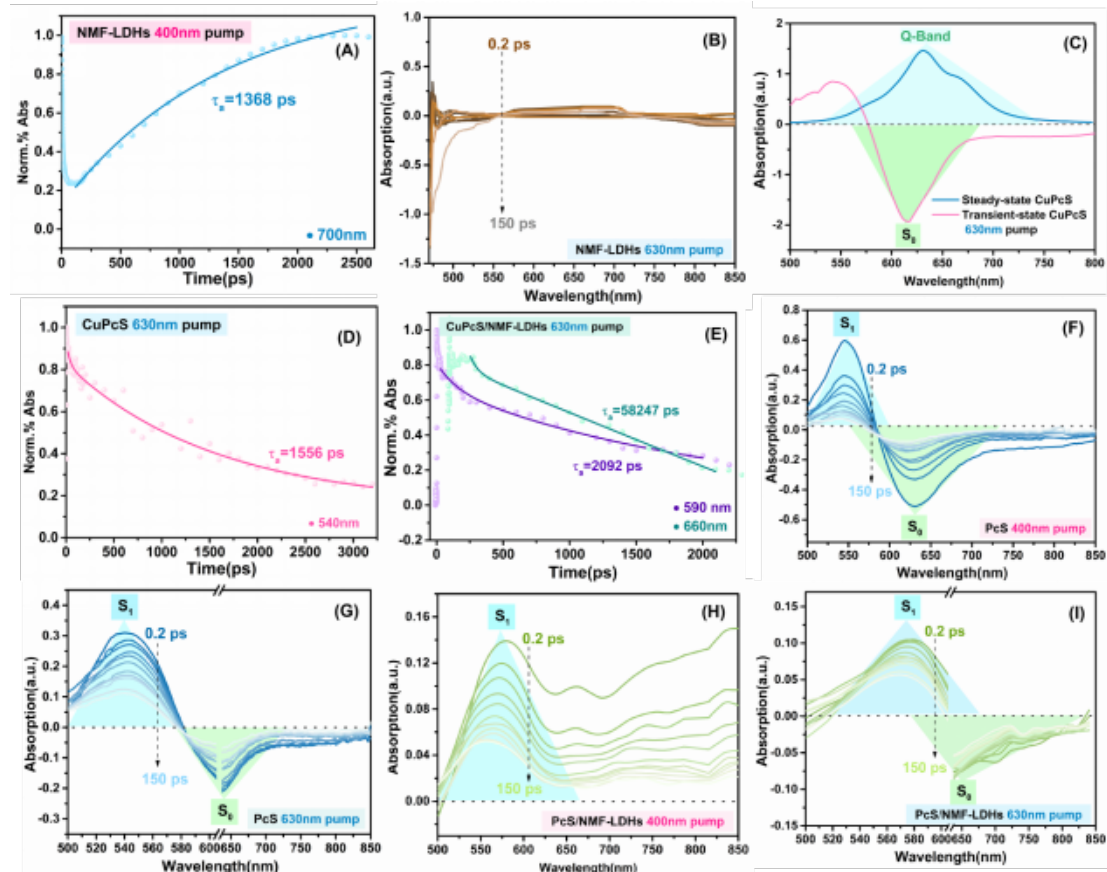


Figure S9. (A) The lifetimes of NMF-LDHs at 700 nm with 400 nm laser excitation by fitting the bi-exponential. (B) TA spectra of NMF-LDHs with 630 nm laser excitation at the different delay times. (C) Comparison of steady-state and transient absorption spectra of CuPcS. The lifetimes of (D) CuPcS and (E) CuPcS/NMF-LDHs with 630 nm laser excitation by fitting the bi-exponential. TA spectra of Pcs with 400 nm laser excitation (F) and 630 nm laser excitation (G) at the different delay times. TA spectra of Pcs/NMF-LDHs with 400 nm laser excitation (H) and 630 nm laser excitation (I) at the different delay times.

The electronic state abbreviations of S_0 , S_1 and T_1 for the Pcs are (π^2) , $^1(\pi, \pi^*)$ and $^3(\pi, \pi^*)$ respectively, and their energies are calculated as follows:

$$E_S = E_0(\pi, \pi^*) + K(\pi, \pi^*) + J(\pi, \pi^*)$$

$$E_T = E_0(\pi, \pi^*) + K(\pi, \pi^*) - J(\pi, \pi^*)$$

$$\Delta E_{ST} = E_S - E_T = 2J(\pi, \pi^*)$$

$E_0(\pi, \pi^*)$ is the excited state zero-level energy obtained from a single electron orbital; $K(\pi, \pi^*)$ is the

electron-electron correlation of the first order Coulomb effect positive; $J(\pi, \pi^*)$ is the correction proposed by Pauli to cause the electron-electron repulsion energy. From this, we can know that the energy difference (ΔE_{ST}) between the S_1 and T_1 of PcS is twice the value of the electron exchange energy $J(\pi, \pi^*)$, which could be calculated the matrix element as follows:

$$J(\pi, \pi^*) = \langle \pi(1)\pi^*(2) | e^2/r_{12} | \pi(2)\pi^*(1) \rangle$$

$$J(\pi, \pi^*) \approx e^2/r_{12} \langle \pi(1)\pi^*(2) | \pi(2)\pi^*(1) \rangle \approx \langle \pi | \pi^* \rangle$$

The magnitude of the exchange energy $J(\pi, \pi^*)$ resulting from electron spin coupling is proportional to the overlap integral, which means that the greater the overlap of the orbitals in space. For the π and π^* orbitals the overlap is large, so the ΔE_{ST} of PcS is relatively large to limit the electrons flip due to such strong electron spin coupling.

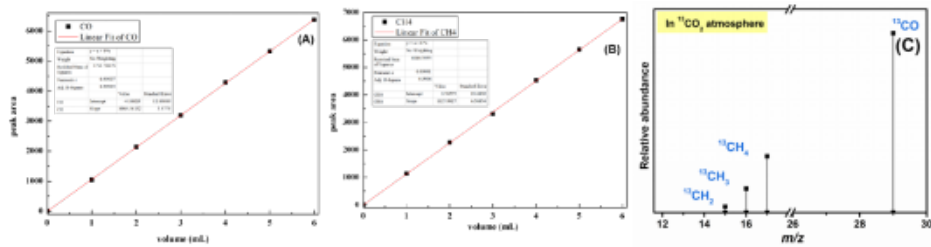


Figure S10. GC standard curve for the quantitative determination of pure (A) CO and (B) CH_4 by external standard method. (C) The isotope experiments of photocatalytic CO_2 reduction with $^{13}\text{CO}_2$.

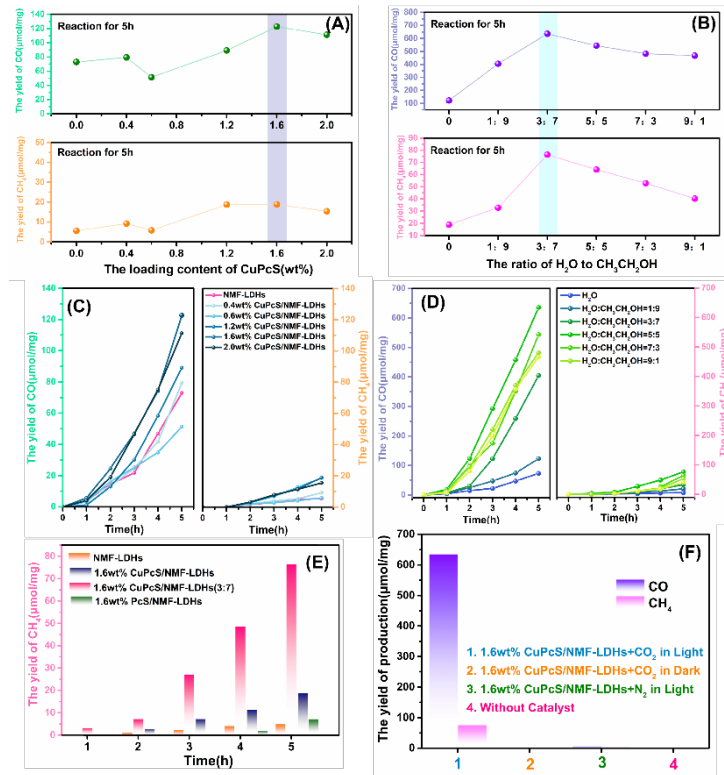


Figure S11. (A) Screening of photocatalytic reduction performance of different concentrations of CuPcS (0.4 wt%, 0.6 wt%, 1.2 wt%, 1.6 wt%, 2.0 wt%) loaded on NMF-LDHs. (B) Selection of photocatalytic reduction performance of CuPcS dissolved in different ratios of solvents (1:9, 3:7, 5:5, 7:3, 9:1) loaded on NMF-LDHs. (C) The yields of CO and CH_4 for NMF-LDHs and different concentrations of CuPcS (0.4 wt%, 0.6 wt%, 1.2 wt%, 1.6 wt%, 2.0 wt%) loaded on NMF-LDHs. (D) The yields of CO and CH_4 for NMF-LDHs and CuPcS dissolved in different ratios of solvents (1:9, 3:7, 5:5, 7:3, 9:1) loaded on NMF-LDHs. (E) The yields of CH_4 for NMF-LDHs, 1.6 wt% CuPcS/NMF-LDHs, 1.6 wt% CuPcS/NMF-LDHs (3:7), and 1.6 wt% PCs/NMF-LDHs within 5 hours. (F)

performing blank and control experiments under the same experimental conditions.

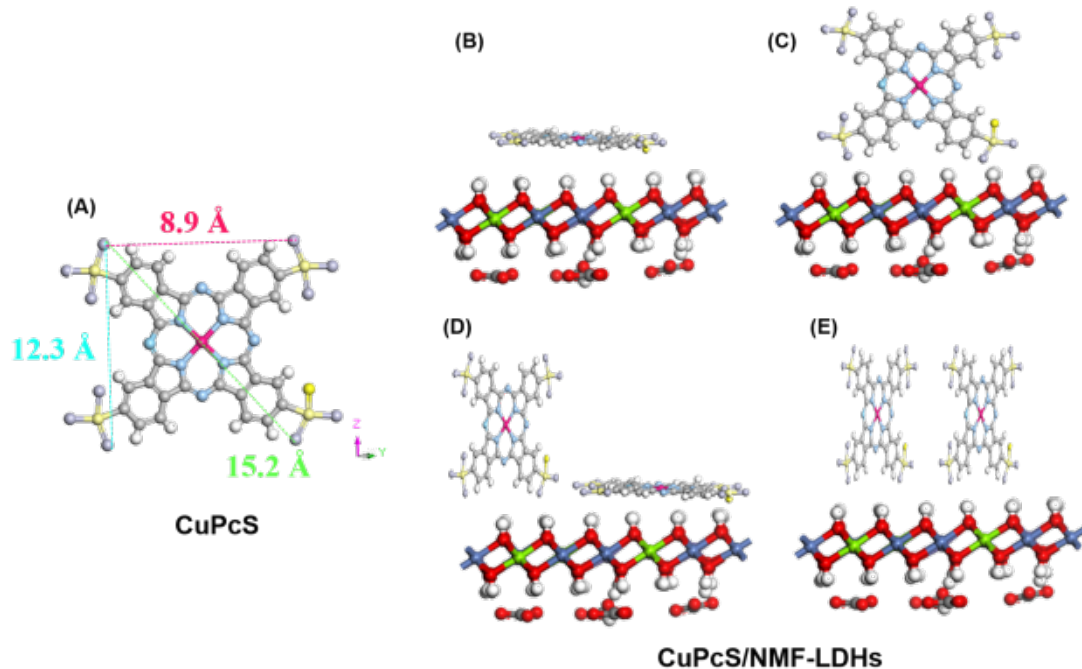


Figure S12. Schematic of the self-assembled molecular orientation of CuPcS with NMF-LDHs. **(A)** CuPcS molecular structure, **(B)** horizontal arrangement, **(C)** vertical arrangement, **(D)** mixed arrangement, **(E)** vertical arrangement of multiple CuPcS.

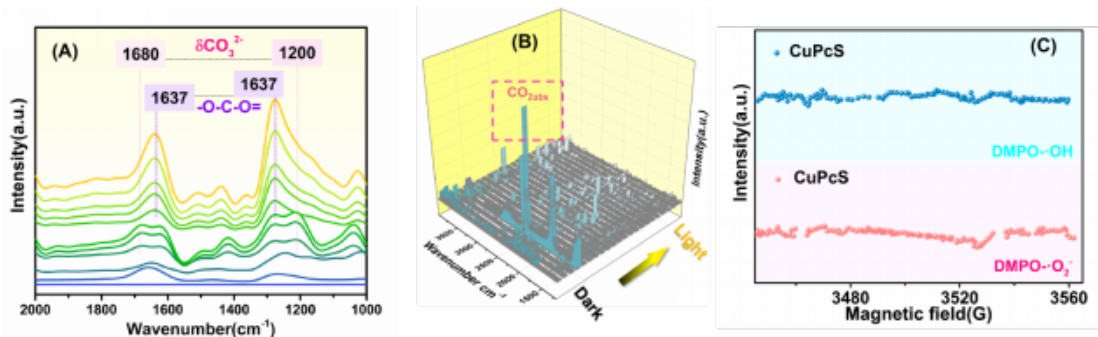


Figure S13. **(A)** The 2D spectra of *in-situ* FTIR of the CuPcS/NMF-LDHs. **(B)** The *in-situ* FTIR of the NMF-LDHs. **(C)** EPR of CuPcS added DMPO to test the ·OH and ·O₂⁻ signals at room temperature.

EPR is measured as the derivative of the absorbed microwave power and so in the absence of resolved nuclear hyperfine coupling, two features will be observed; a smaller positive going feature corresponding to molecules aligned with their axis parallel to the magnetic field which is referred to as $g\parallel$ and a second stronger feature that appears similar to a 1st derivative Gaussian line from molecules oriented with their symmetry axis perpendicular to the applied magnetic field. We will refer to this feature as coming from $g\perp$. The CuPcS is planar aromatic molecule, and axial symmetry is reflected in EPR spectra, with g being axially symmetric. Although there are two isotopes, ⁶³Cu and ⁶⁵Cu which both have a nuclear spin of 3/2 giving rise to four distinct energy levels, we did not observe the hyperfine structure of 3100 G for the $g\parallel$ (1.999) because it was not well distinguished in polycrystalline samples.

Reference

1. C. Cheng, L. Mao, X. Kang, C.-L. Dong, Y.-C. Huang, S. Shen, J. Shi and L. Guo, *Applied*

- Catalysis B: Environmental*, 2023, **331**, 122733.
- 2. Z. Zhao, D. Zheng, M. Guo, J. Yu, S. Zhang, Z. Zhang and Y. Chen, *Angewandte Chemie International Edition*, 2022, **61**, e202200261.
 - 3. H. Kumagai, Y. Tamaki and O. Ishitani, *Accounts of Chemical Research*, 2022, **55**, 978-990.
 - 4. S. Kang, Z. Li, Z. Xu, Z. Zhang, J. Sun, J. Bian, L. Bai, Y. Qu and L. Jing, *Catalysis Science & Technology*, 2022, **12**, 4817-4825.
 - 5. A. Kumar, P. K. Prajapati, M. S. Aathira, A. Bansiwal, R. Boukherroub and S. L. Jain, *Journal of Colloid and Interface Science*, 2019, **543**, 201-213.
 - 6. Z. Mu, S. Chen, Y. Wang, Z. Zhang, Z. Li, B. Xin and L. Jing, *Small Science*, 2021, **1**, 2100050.
 - 7. B. Li, L. Sun, J. Bian, N. Sun, J. Sun, L. Chen, Z. Li and L. Jing, *Applied Catalysis B: Environmental*, 2020, **270**, 118849.
 - 8. J. Bian, J. Feng, Z. Zhang, J. Sun, M. Chu, L. Sun, X. Li, D. Tang and L. Jing, *Chemical Communications*, 2020, **56**, 4926-4929.
 - 9. J. Bian, L. Sun, Z. Zhang, Z. Li, M. Chu, X. Li, D. Tang and L. Jing, *ACS Sustainable Chemistry & Engineering*, 2021, **9**, 2400-2408.